nature communications

Article

https://doi.org/10.1038/s41467-025-66061-8

Transcytotic transportation of size-controlled nanocarriers into dystrophic skeletal muscle leads to therapeutic outcome in mice

Received: 21 April 2025

Accepted: 24 October 2025

Published online: 11 December 2025

Check for updates

Xiangsheng Liu[1,10], Michael R. Hicks[2,10], Zhenhan Feng[3,4,10], Jinhong Jiang[1,10], Yuting Li[1], Courtney S. Young[5], Tianyu Zhang[1,4], Kholoud Saleh[6], Michael R. Emami[7], Yanyan Liu[3], Mengmeng Qin[3], Jiulong Li[3], Yile Zheng[1,4], Honghong Yang[1], Melissa J. Spencer[7,8,9] ✉, April D. Pyle[6,8,9] ✉ & Huan Meng[3,4] ✉

Duchenne Muscular Dystrophy (DMD) is a lethal muscle-wasting disorder with limited therapeutic options. Although nano drug delivery offers promise, the biodistribution and access routes to dystrophic muscle remain poorly understood. Here we show that intravenously administered mesoporous silica nanoparticle (MSNP) carriers exhibit striking size-dependent biodistribution in male DMD mice. Small nanocarriers (50-100 nm) efficiently accumulate in skeletal muscle while avoiding hepatic and splenic sequestration, outperforming larger particles (200-300 nm). Importantly, we uncover that endothelial transcytosis, not passive vascular leakage, is the dominant and previously unrecognized route by which nanocarriers access dystrophic muscles. Further, we encapsulate tamoxifen, a repurposed drug, into optimized MSNPs. This intervention increases utrophin expression, reduces fibrosis, and diminishes myofiber necrosis, resulting in improved muscle health and strength. Our results establish size-tuned, transcytosis-enabled nanocarriers as a transformative strategy for targeted drug delivery to dystrophic muscle, paving the way for nanomedicine-based therapies in DMD and potentially other muscle disorders.

In the past few decades, different nanocarriers have been developed and tested in experimental animals and patients[1,2]. Despite many nanocarriers being tested in various diseases such as cancer, the neuromuscular field has not witnessed success with systemically delivered nanoparticles (NPs). For example, in diseases such as Duchenne muscular dystrophy (DMD)[3–5], the carriers need to efficiently deliver cargo to all muscles of the body. DMD is an X-linked muscle-wasting disorder characterized by progressive muscular

[1]Zhejiang Cancer Hospital, The Key Laboratory of Zhejiang Province for Basic and Clinical Application of Functional Nucleic Acids, Hangzhou Institute of Medicine, Chinese Academy of Sciences, Hangzhou, Zhejiang, China. [2]Department of Physiology & Biophysics, University of California, Irvine, CA, USA. [3]CAS Key Laboratory for Biomedical Effects of Nanomaterials and Nanosafety and CAS Center for Excellence in Nanoscience, National Center for Nanoscience and Technology, Beijing, China. [4]University of Chinese Academy of Sciences, Beijing, China. [5]MyoGene Bio, San Diego, CA, USA. [6]Department of Microbiology, Immunology and Medical Genetics, David Geffen School of Medicine at UCLA, Los Angeles, CA, USA. [7]Department of Neurology, David Geffen School of Medicine at UCLA, Los Angeles, CA, USA. [8]Eli and Edythe Broad Center of Regenerative Medicine and Stem Cell Research at UCLA, Los Angeles, CA, USA. [9]Center for Duchenne Muscular Dystrophy at UCLA, Los Angeles, CA, USA. [10]These authors contributed equally: Xiangsheng Liu, Michael R. Hicks, Zhenhan Feng, Jinhong Jiang. ✉e-mail: MSpencer@mednet.ucla.edu; Apyle@mednet.ucla.edu; Mengh@nanoctr.cn

weakness[6]. Recently, Elevidys, an adeno-associated virus vector-based (AAV) gene therapy, was approved to treat pediatric patients with DMD[7]. However, the high dose of AAV could be associated with potential side effects, and the generation of neutralizing antibodies may limit repeated administrations of AAV[8]. Therefore, in addition to the viral carrier, there is considerable interest in developing non-viral carriers for DMD therapy.

The concept of a nano-enabled delivery system is an exciting development that holds promise for treating DMD. This includes the encapsulated delivery of various active pharmaceutical ingredients (APIs), such as small molecules, nucleic acids, and gene editing platforms[3,9,10]. While various lipid- and polymer-based nanomaterials have been tested, there has been limited success in achieving efficient systemic delivery in preclinical models[3,9,10]. It was demonstrated that a ~15 nm cationic nano gold-based gene editing platform could successfully deliver Cas9 RNPs and donor DNA through intramuscular administration in a DMD mouse model[11]. Intramuscular injection of RNPs carrying CRISPR/Cas9 led to detectable editing of the *Dmd* gene. While these results are promising, achieving systemic delivery to multiple muscles in DMD remains a tremendous challenge to overcome, considering there are over 640 skeletal muscles that comprise 40–50% of body mass[12–14].

An intriguing question surfaces: How do nanoparticles, administered systemically, traverse the endothelial barrier to reach the muscle tissues from the bloodstream? Understanding the mechanisms could offer valuable insights to enhance nanoparticle-mediated systemic delivery. Systemically delivered nanocarriers must first interact with the vasculature before entering tissues and reaching the muscle sites. Compared to solid tumors that have been extensively studied[15–19], the interactions with blood vessels in muscle tissues remain largely unknown. Our laboratory developed an ultrastructural transmission electron microscopy (TEM) procedure to investigate nanoparticle tumor access. This technique can differentiate between enhanced permeability and retention (EPR) effect versus the transcytosis transport pathway in a Kas-mutated pancreatic cancer model[15,20]. We also reported that tumor transcytosis is regulated by neuropilin-1, which is a physiological process needed for nutritional supply[15]. Recently, more evidence demonstrated the important role of transcytosis in the entry of nanoparticles into stroma-rich solid tumors[16–18,21–23].

Considering the dynamic environment of dystrophic muscles, DMD shares certain similarities with solid tumors, such as a fibrotic and inflamed microenvironment, high metabolic demand, and increased pericyte coverage of the blood vessels[24–26]. These resemblances have motivated us to develop imageable nanocarriers for investigating the mechanism of systemic nanoparticle delivery in dystrophic muscles. Given that NP sequestration by the reticuloendothelial system (RES) in DMD animal models has often been overlooked, we also examine the RES uptake of NPs in comparison to the homing efficiency in DMD muscles. A remarkable finding using the TEM-imageable gold-labeled model NP is that IV-injected NP utilizes a vascular transport pathway through endothelial cells (ECs) in muscles. We have conducted transcytosis experiments at multiple levels: intact animal level (IVIS imaging, together with a "Zombie" interference experiment), cellular level using sorted muscle ECs (>8000 sorted cells per sample), and ultrastructural level (73 blood vessels region-of-interests from 3 mice and 3 muscle types). Drawing upon these extensive datasets, we have reached the conclusion that transcytosis plays a critical role in facilitating NP access to dystrophic muscles. This discovery offers valuable insights into the underlying mechanisms and biological processes involved in DMD systemic drug delivery. As a proof-of-concept, we further utilize the transcytotic mechanism for the systemic delivery of tamoxifen (TMX), an example cargo that is originally an anticancer drug but has been repurposed for DMD[27–29]. In male DMD mice, TMX NPs lead to increased utrophin expression in the gastrocnemius and triceps muscles, reduced fibrosis in the gastrocnemius, triceps, and quadriceps, and decreased necrosis in the gastrocnemius and quadriceps. Additionally, muscle strength function is also improved using TMX NPs.

Results

Synthesis of a biocompatible nanocarrier library identifies size-dependent systemic homing to dystrophic muscles

Key impediments to employing nanocarriers for effective drug delivery in DMD have included a lack of understanding of how the physicochemical characteristics of engineered NPs (e.g., size, colloidal stability, surface chemistry, etc.) impact biodistribution, pharmacokinetic (PK), RES sequestration, and ultimately efficacy and safety. While the effect of size has been intensively studied in non-dystrophic animals, a systematic dissection of the effect of size on biodistribution has not been previously reported in dystrophic mice. Fig. 1A depicts a schematic illustrating the structure of a lipid-coated mesoporous silica nanoparticle (MSNP). This drug delivery platform has been established to facilitate systemic delivery of small molecules, nucleic acids, proteins, peptides, and their combinations[15,30–37]. Four size-controlled MSNP cores were selected for synthesis at primary particle sizes of ~50 nm, ~100 nm, ~200 nm, and ~300 nm. This was achieved through a seed-growth process by first making 50 nm bare MSNPs using a sol-gel chemistry[30,31,38], and then using them as cores to further grow the larger particles[39,40]. In order to obtain colloidally stable particles, the MSNP surface was further coated by a phospholipid bilayer that contains 1,2-distearoyl-sn-glycero-3-phosphocholine (DSPC): cholesterol (Chol): 1,2-distearoyl-sn-glycero-3-phosphoethanolamine-N-[methoxy (polyethylene glycol)−2000] (DSPE-PEG2000) = 60:40:3 molar ratio[31]. Bare and lipid-coated MSNPs were characterized by TEM (Fig. 1B, upper panel) and cryogenic electron microscopy (cryo-EM) (Fig. 1B, lower panel) to assess the primary particle size, morphology, and surface coating integrity. This allowed us to show MSNP core primary sizes of 47.5 ± 6.6–301.6 ± 11.2 nm (Fig. 1C). Cryo-EM data confirmed that there was uniform lipid coating on all 4 samples; the thickness of the coating was 6–7 nm (Fig. 1B, lower panel). The hydrodynamic size of the lipid-coated version was 93.1 ± 1.6–382.1 ± 4.0 nm (Fig. 1C). All the samples exhibited a slightly negative charge at the physiological pH 7.4, with a ζ-potential value of −11 to −15 mV (Fig. 1C).

To track the biodistribution of MSNPs at the tissue and cellular level in dystrophic muscles, we covalently labeled the MSNPs with a near-infrared (NIR) dye, DyLight 680 (Dy680), with $\lambda_{ex/em}$ of 692 nm/712 nm. The fluorescence spectra of the labeled NPs demonstrated similar labeling efficiency at identical concentration (Supplementary Fig. 1), which enabled us to semi-quantitatively compare their in vivo biodistribution. We designated the NIR-labeled lipid-coated nanoparticles with controlled sizes as $NP_{50\,nm}$, $NP_{100\,nm}$, $NP_{200\,nm}$, and $NP_{300\,nm}$.

To evaluate NPs' biodistribution, male dystrophic mice (~3 months) received a single intravenous (IV) injection of 10 mg/mL NIR dye-labeled NPs with different size ranges at 50 mg/kg particle dose through the tail vein. All mice survived IV injections and were sacrificed at 24 h. Skeletal and cardiac muscles were dissected and immediately imaged ex vivo using an IVIS imaging system (Fig. 1D). Contrary to previous reports on the impenetrable anatomy of skeletal muscle to nanoparticles in the wild-type (WT) animals[13,41], we observed significant nanocarrier access in the dystrophic muscles. Both 50 nm and 100 nm NPs showed strong NIR fluorescence intensity in upper and lower limb skeletal muscles, including gastrocnemius, quadriceps, and triceps. $NP_{50\,nm}$ and $NP_{100\,nm}$ samples were also significantly increased in the diaphragm and tibialis anterior muscles relative to other sizes. Conversely, mice receiving $NP_{200\,nm}$ and $NP_{300\,nm}$ showed less abundance in skeletal limb muscles and limited signal in the diaphragm and heart.

In addition to muscles, we also harvested the major organs from the same mice, including the RES organs (such as liver and spleen),

https://doi.org/10.1038/s41467-025-66061-8

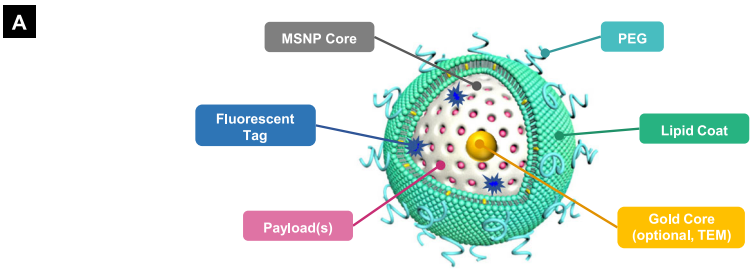

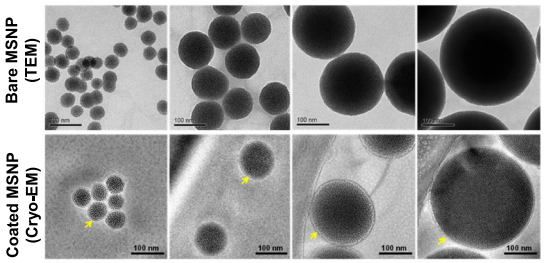

C

Sample	MSNP core size (TEM, nm)	Hydrodynamic size (DLS, nm)	Hydrodynamic size PDI	Zeta potential (mV)
$NP_{50\ nm}$	47.5 ± 6.6	93.1 ± 1.6	0.080	-15.1 ± 0.7
$NP_{100\ nm}$	104.2 ± 7.2	155.5 ± 0.6	0.030	-14.8 ± 1.4
$NP_{200\ nm}$	193.7 ± 6.8	266.5 ± 3.9	0.069	-11.0 ± 1.6
$NP_{300\ nm}$	301.6 ± 11.2	382.1 ± 4.0	0.020	-12.0 ± 1.1

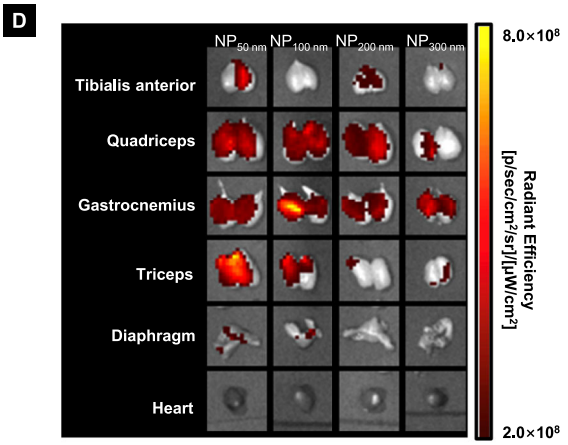

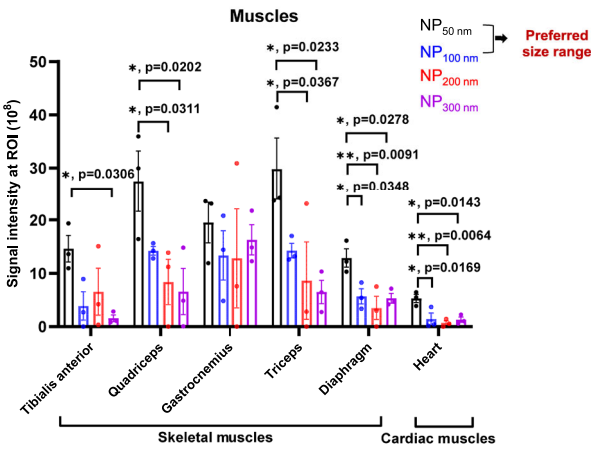

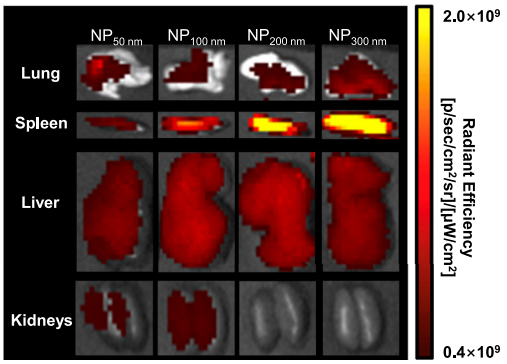

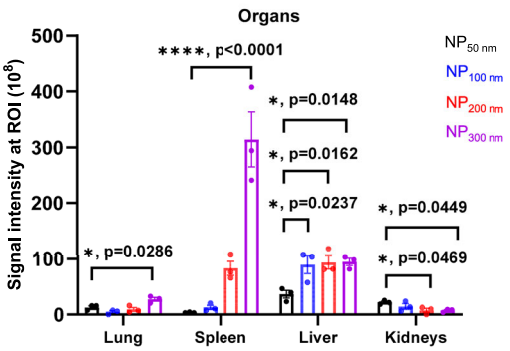

Fig. 1 | Size-dependent biodistribution of NPs in dystrophic muscles. A Scheme of the multifunctional nanocarrier used in this study, which is comprised of an MSNP core that contains a large packaging space for payloads and surface coated with an intact lipid bilayer (LB) with high colloidal stability and long circulatory half-life. MSNP can be labeled with fluorescence dyes or a gold nanoparticle core for optical or TEM imaging. **B** TEM images of different sizes of bare MSNPs (upper panel) and cryo-EM images of MSNPs after LB coating. Two independent experiments were performed with similar results. **C** DLS hydrodynamic size, polydispersity index (PDI), and zeta potential of the LB-coated different-sized MSNPs in PBS. Ex vivo NIR fluorescence imaging of muscles (**D**) and organs (**E**) at 24 h after dystrophic mice (mdx, ~3 months) received IV injection of NIR-labeled LB-coated MSNPs with different sizes but at the same particle dose (50 mg/kg). NIR fluorescence intensity at the region-of-interest (ROI) was used to quantify the NP content in different muscles and organs. Data represent mean ± SEM ($n = 3$ mice). $^{*}p < 0.05$, $^{**}p < 0.01$, $^{****}p < 0.0001$ compared to 50 nm NP group, one-way ANOVA followed by Dunnett's test. Source data are provided as a Source data file.

kidneys, and lungs. We observed a contrasting trend in that $NP_{200\,nm}$ and $NP_{300\,nm}$ nanoparticles were dramatically sequestered in RES organs (Fig. 1E). This was especially true of the spleen, which showed a significant size-dependent accumulation, where the accumulation of $NP_{300\,nm}$ was about 20-fold and 80-fold higher than the $NP_{100\,nm}$ and $NP_{50\,nm}$ treatments, respectively. Given our preference for nanocarriers with high muscle uptake and low RES capture, we have deduced that the size range between $NP_{50\,nm}$ and $NP_{100\,nm}$ could be optimal.

Ultrastructural analysis of nanoparticle transportation through a transcytosis process across endothelial cells

As it has been demonstrated numerous times that IV-injected nanocarriers do not abundantly biodistribute to skeletal muscle in healthy WT mice[13,14,42–44], we set out to identify the mechanism for enhanced nanoparticle retention in dystrophic muscles. Through our size-dependent studies in the DMD preclinical model, we have pinpointed the optimal size range for biodistribution to be 50–100 nm MSNP core. However, we also acknowledge that smaller particle sizes are usually linked to lower loading capacity. Therefore, we made the decision to utilize an intermediate particle size of approximately 70 nm core (Fig. 2A) for mechanistic NP muscle access investigations (Figs. 2 and 3), followed by a proof-of-concept drug delivery study (Fig. 4).

We synthesized NIR dye-labeled NPs (using ~70 nm MSNP core), whose fluorescence properties enabled us to visualize their localization using confocal microscopy alongside multi-color immunofluorescence (IF) muscle staining in tissue sections (Fig. 2A, left). Moreover, we also synthesized ~70 nm MSNPs with a ~10 nm gold core, which could be in situ visualized due to the unique core/shell nanostructure and the high electron density of gold under tissue TEM (Fig. 2A, right). The hydrodynamic DLS size and ζ-potential value for both imageable particles were ~130 nm and ~−10 mV, respectively.

To validate the findings in Fig. 1 and additionally investigate the time-dependent particle muscle homing, NIR-labeled NPs were IV administered (50 mg/kg) via the tail vein in male DMD mice. The mice were then sacrificed at 1, 4, and 24 h, and muscle samples were immediately harvested. This experiment confirmed an effective biodistribution of NP in dystrophic muscles, revealing a noticeable trend of time-dependent NP accumulation inside various muscles (Fig. 2B). To determine whether the nanoparticles were trapped in muscle vasculature or the interstitial space, muscle tissues were collected for histological analysis. Immunofluorescence (IF) staining was used to label collagen IV (in the basement membrane surrounding muscle fibers) and CD31 (an EC marker revealing the vasculature), enabling us to look at NP distribution (Fig. 2C). Visual analysis of NIR fluorescence distribution using confocal microscopy provided clear evidence of nanocarrier extravasation in dystrophic muscles. Additional ex vivo IVIS and confocal imaging further confirmed the preferential retention of NPs in dystrophic muscles but not in the healthy muscles (Supplementary Fig. 2). Interestingly, the accumulations of NPs in liver and spleen at 24 h postinjection were both significantly lower (~50% and ~30% reduction, respectively) in dystrophic mice compared to those in WT animals (Supplementary Fig. 2A). We speculate that one possible reason is the competitive retention of NPs within dystrophic muscles. This may reduce the likelihood of long-circulating NPs being captured by the RES, such as the liver and spleen. Other factors might also contribute. Moreover, to understand the influence of age, we also conducted a comparative analysis of NP distribution between young (8-week-old) and aged (30-week-old) WT and dystrophic mice. This analysis was performed 24 h after the IV injection of same labeled NPs as we described in Fig. 2. The results verified the substantial accumulation of NPs in the skeletal muscles of both young and aged mice, with minimal accumulation observed in WT mice in both ages (Supplementary Fig. 3). This finding aligned with our recent research, which demonstrated the retention of particles in various DMD models[45].

While the literature reported that different nanocarriers were injected into DMD mice[3,9,46,47], the exact nanocarrier transport mechanism remains largely unknown in skeletal muscle, an organ that usually does not correlate with EC permeability[48]. Therefore, we conducted a repeat of the IV injection experiment using gold-labeled NPs, and after 24 h of IV injection, muscles such as gastrocnemius (G), quadriceps (Q), and triceps (T) were harvested and used for TEM visualization. Although we have provided semi-quantification for TEM pictures later (see Fig. 3), we were able to occasionally visualize the involvement of a leaky fenestration (resembling EPR) and, surprisingly, the more often identification of nanoparticle transcytosis in dystrophic muscles.

To illustrate these two distinct mechanisms of nanoparticle entry to muscle, we have provided three representative blood vessels (Fig. 2D). The dystrophic muscle microenvironment where nanoparticle transportation occurs is heterogeneous due to chronic degeneration and regeneration. TEM pictures of vessels #1 and #2 were obtained at high magnification (Fig. 2D), where we observed ECs, pericytes (PC), red blood cells (RBCs), collagen deposition, and myofibers (MF). The TEM images allowed us to visualize NPs within the lumen of a blood vessel as well as their deposition in the interstitium. An intriguing and frequent observation was nanoparticle transport via a trans-EC process without the requirement of vessel leakiness. We found that numerous NPs were taken up through a process of EC transcytosis, evident by continuous and stepwise procedures, including the presence of cell membrane extrusion, filopodia interacting with NPs, formation of intra-EC vesicles (that co-localize with the NPs), and the subsequent release of NPs into the muscle interstitium (exocytosis). Specially, in the vessel #1 (Fig. 2D, middle panel), we illustrated the early stage (i.e., particle/filopodia interaction), and in the vessel #2 (Fig. 2D, right panel), we showed the intermediary/late stage (i.e., trans-EC transport and exocytosis). The zoomed-in pictures for individual NP, labeled as “α,” “β,” “γ,” and “μ,” which contained the gold-core labeling, allowed us to identify these NPs at ultrahigh resolution in the TEM images. We saw similar NP transcytosis features at early time points (1 and 4 h), confirming that this effect occurred as early as 1 h post IV injection (Supplementary Fig. 4).

TEM also revealed that NPs’ access to muscle tissues via leaky blood vessels, through enlarged fenestrations, but this occurred much less frequently. This process is exemplified in the case of vessel #3 (Fig. 2E). From left to right, with increased magnification, we demonstrated the presence of NPs in the lumen of a blood vessel (circulating NPs, such as “ρ” in Fig. 2E) and the deposition of NP in the interstitium (extravasated NPs, such as “π” in Fig. 2E), adjacent to the enlarged fenestrations (“leaky site”) in the EC. Similar to Fig. 2D, we could identify the individual NP through the unique core/shell structure under TEM. Another infrequent but detectable event was NP internalization in myofibers (Fig. 2F). Although this aspect is beyond the scope of the current research, it does open the possibility of utilizing our nanocarrier for gene therapy applications. However, achieving this may require additional iteration. In addition, we also conducted a comparative TEM analysis illustrating the blood vessels in WT mice. As expected, there were significantly fewer morphological features associated with NP transcytosis (e.g., filopodia engulfment, vesiculo-vacuolar organelles (VVOs) formation, and exocytosis) in the blood vessels of WT mice (Fig. 2G). Although some circulating nanoparticles were observed in the vascular lumen of WT mice, their internalization within ECs was minimal. This finding aligns with the minimal muscle uptake observed in WT mice receiving various types of nanoparticles[14,44].

TEM is a prevalent approach for studying nanoparticle transport (usually in cancer scenarios)[15,18]; however, logistical limitations inherent to tissue TEM often lead to relatively small sample sizes[18]. To

https://doi.org/10.1038/s41467-025-66061-8

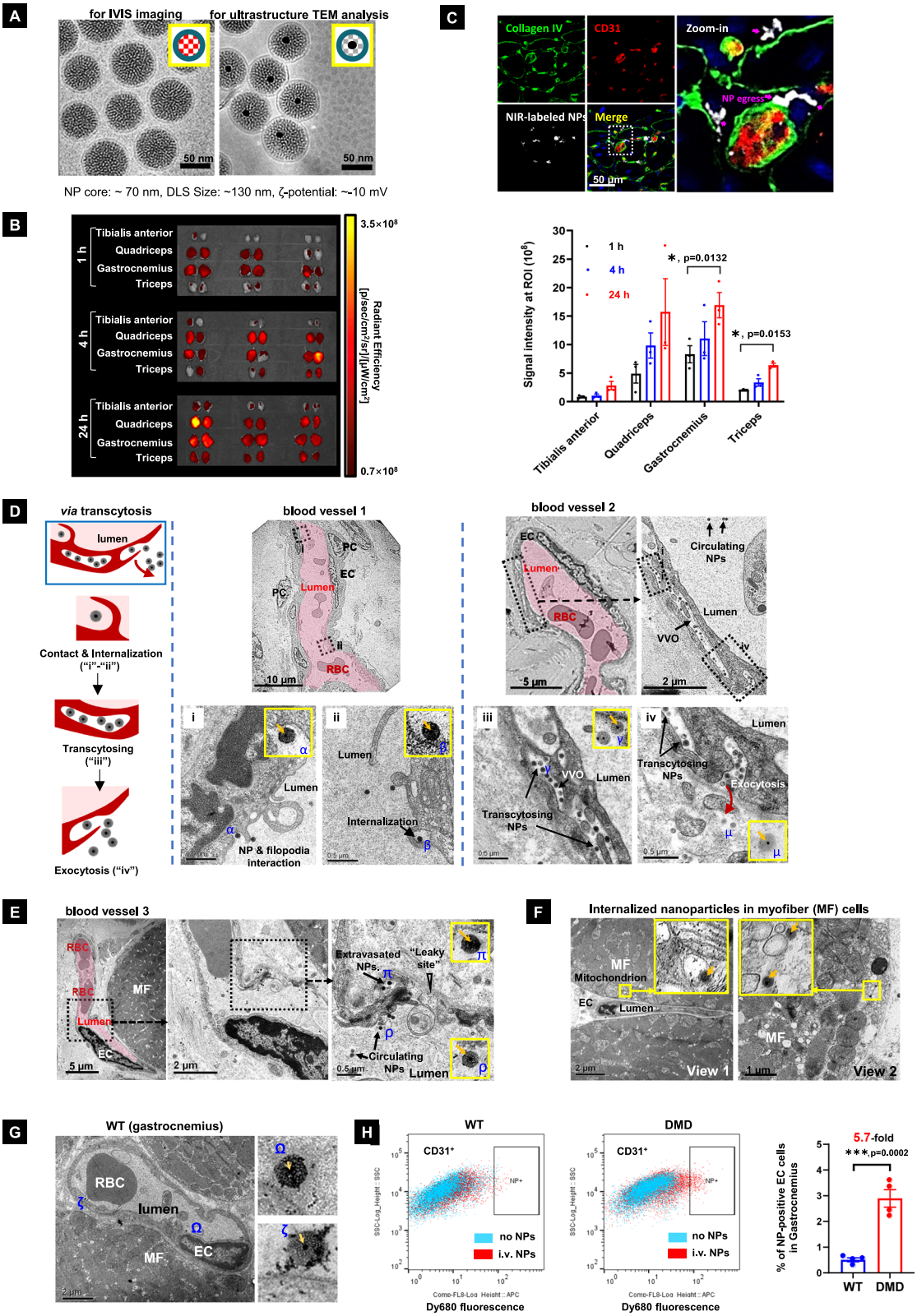

address this limitation, we first employed a flow cytometry-based technique to examine NP distribution in ECs from the gastrocnemius muscle of mice, dosed IV with Dy680-labeled nanoparticles; WT animals served as the control group (Fig. 2H). Given that only transcytotic NPs internalize and traffic intracellularly, we anticipate that transcytosis-involved EC should be detectable by flow cytometry. In contrast, NPs that enter tissues by extravasation (i.e., that enter tissues through leaky sites) should not be detected within ECs. Our data showed that the abundance of Dy680^{positive} EC cells was 5.7-folder higher in dystrophic muscles compared to WT mice (Fig. 2H). The flow cytometry gating strategy and the original data for each mouse are available online (Supplementary Fig. 5). Based on this flow data collected from four mice per group, involving over 32,000 EC counts ($n = 4$, >8000 ECs/mouse), we have strong evidence of robust NP

Fig. 2 | Systemically administered NPs biodistribute to dystrophic muscles. **A** Cryo-EM images of NIR-labeled or gold-embedded NPs. Bars are 50 nm. Two independent experiments were performed with similar results. **B** Biodistribution study using NIR-labeled NP in dystrophic mice (B10-Dmd-KO) at the indicated time points. Data represent mean ± SEM ($n = 3$ mice). *$p < 0.05$, one-way ANOVA followed by Dunnett's test. **C** Confocal microscopy to show the intramuscular distribution of the NIR NPs in the gastrocnemius of mdx mice at 24 h postinjection. Red, CD31; green, collagen IV; blue, DAPI; gray, NIR particles. Bar represents 25 μm. **D** Gold-embedded NPs were used to study nanocarrier access in mdx mice. In the vessel #1, zoom-in images show the internalization of NPs from the vascular lumen by EC, including (i) cell membrane extrusion to form filopodia and NPs interacting with filopodia, and (ii) NPs engulfed by EC. In the vessel #2, zoom-in images demonstrate the process that (iii) intracellular transport stage of NPs located in the transcytotic vesicles and (iv) exocytosis of NPs (red arrows) from EC to muscle matrix. Ultrahigh resolution pictures for individual NP, "α," "β," "γ," and "μ," confirm the presence of a gold core. **E** Representative images showing the possible extravasation of NPs from a leaking vessel with a gap between endothelial cells. While particle "ρ" was in the circulation, "π" was extravasated into the tissue matrix. EC endothelial cell, F filopodia, L lumen, PC pericyte, RBC red blood cell, CM cell membrane, MF myofiber. **F** NP uptake inside myofiber cells. **G** TEM images of the gastrocnemius muscle from WT mice following IV administration of gold-embedded lipid-MSNPs at 24 h. Circulating NPs in the blood vessel lumen were shown, i.e., particles "Ω" and "ζ." No transcytosis feature was observed. For (**C**–**G**), the data were representative of three independent experimental replicates with similar results. **H** Flow cytometry analyzing NP^+ EC in the gastrocnemius muscle of dystrophic (B10-Dmd-KO) vs WT mice received IV Dy680-labeled NPs. The % $CD31^+Dy680^+$ cells were counted. Data represent mean ± SEM ($n = 4$ mice, >8000 cell count per mouse). ***$p < 0.001$, two-tailed Student's t-test. Source data are provided as a Source data file.

transcytosis in dystrophic blood vessels. This discovery has motivated us to explore the extent of transcytosis in NP transportation, essentially probing whether transcytosis plays a primary role in the dystrophic muscle site.

High frequency of transcytosis was responsible for nanoparticle accumulation in dystrophic muscles

While flow cytometry analysis suggests a role for transcytosis in nanoparticle entry into dystrophic muscles, we aimed to investigate this mechanism in greater ultrastructural detail and quantify it to the maximum extent possible. While challenging, we advocate the use of complementary methodologies to study NP transcytosis using combined TEM analysis at ultrastructural resolution (Fig. 3A) and "Zombie" model at intact animal level (Fig. 3C). Accordingly, we first performed IV injections in 3 dystrophic mice and analyzed 3 different muscle types (gastrocnemius, quadriceps, triceps) 24 h post IV injection. Among the 73 regions-of-interest (ROIs) that were collected, 37 vessels from gastrocnemius (G), 28 vessels from quadriceps (Q), and 8 vessels from the triceps (T) were analyzed (Fig. 3B1). A comprehensive summary of all the vessels, assigned with unique identifiers and muscle type information, along with the original TEM images captured at different magnifications, showcasing the key features involved in the NP transportation process, can be found online (Supplementary Data 1). From a morphological perspective, we examined six distinct features, including (i) circulating NPs inside blood vessels (Fig. 3B2), (ii) NP internalization into EC cells (Fig. 3B3, 2nd column), (iii) NP inside intra-EC vesicles (Fig. 3B3, 3rd column), (iv) NP exocytosis from ECs (Fig. 3B3, 4th column), and (v) extravasated NPs adjacent to large fenestrations (Fig. 3B4). We also examined already-transported NPs outside the blood vessels, as the sixth morphological feature (Fig. 3B5). We counted the number of blood vessels exhibiting these features in Fig. 3B3, namely EC internalization + NPs in EC vesicles + exocytosis, as blood vessels involving transcytosis. Additionally, we calculated the number of blood vessels involved in particle leakage through enlarged fenestrations (Fig. 3B4). In the total 73 vessels examined, 41 out of 73 blood vessels involved transcytosis, whereas 5 out of 73 blood vessels involved leakage (Fig. 3B6). In the gastrocnemius, quadriceps, and triceps, transcytosis-positive vessels account for 54% (20 out of 37), 53% (15 out of 28), and 75% (6 out of 8), respectively, while leaky vessels only represent 3%, 14%, and 0% in these muscle types. Based on this analysis, the chance of identifying transcytosis is 8.2-fold higher than EPR in all three muscle types we observed in dystrophic mice. Another impression was that most NPs were free and not captured by the phagocytic cells inside the bloodstream. This observation contrasts with what was noted in WT animals, where the presence of blood vessels containing nanoparticles with transcytosis features is minimal (see Fig. 2G and Supplementary Data 2).

To further illustrate the predominant role of transcytosis at the intact animal level, we conducted a "Zombie model" experiment. This experimental design, originally intended for tumor transcytosis[18], was employed to showcase transcytosis in the DMD mouse model. As the "Zombie" mice were fixed and subjected to NP circulation using a peristaltic pump, the expectation was to impede active transcytotic delivery while retaining NP leakage through blood vessels. Two hours post NIR-labeled NP circulation, we observed a substantial fluorescent signal decrease of 71%, 64%, and 66% in quadriceps, gastrocnemius, and triceps in the "Zombie" dystrophic mice compared to control (Fig. 3C). This data served as additional evidence supporting the predominant role of NP transcytosis in dystrophic mice.

We have demonstrated the pivotal role of NP transcytosis in ECs, which frequently involves various membrane-associated signaling cascades, including actin polymerization and plasma membrane ruffling. In light of the quantitative flow cytometry data in Fig. 2H, we conducted IV nanoparticle administration in dystrophic mice, sacrificed the mice 24 h postinjection, and performed cell sorting to distinguish between the $CD31^+NP^+$ (transcytosing ECs) and $CD31^+NP^-$ ("quiescent" ECs) populations. This was followed by an RNA sequencing experiment (Fig. 3D). Differential gene expression in transcytosing ECs compared to "quiescent" ECs was shown in the Volcano plot (Fig. 3D1). We identified 50 up-regulated genes and 199 down-regulated genes. The top 25 most differentially expressed genes in transcytosing ECs were listed in the heatmap (Fig. 3D2), among which we identified several genes related to the activation of guanosine triphosphate (GTP)-binding proteins according to the NCBI information. The Rragd (Ras-related GTP binding D) and Depdc1a (DEP domain containing 1a) are related to GTPase binding activity, and Cadm4 (cell adhesion molecule 4) is able to regulate Rac protein signal transduction. From a functional perspective, these gene targets, which are linked to small GTPase activity, could play important roles during transcytosis, such as membrane ruffling, cytoskeletal changes, and the closure of macropinosomes[49]. Besides the most differentially expressed genes in the heatmap, we also observed upregulation of several transcytosis-related genes, including Plvap, Lrp10, and Selp, in NP^+ ECs, consistent with findings reported in the transcytosis literature (Fig. 3D3)[19]. To investigate whether endothelial dystrophin deficiency contributes to the differential nanoparticle uptake observed in DMD mice, we also performed comparative transcriptomic profiling of ECs isolated from DMD and WT mice, in the absence of nanoparticle exposure (Supplementary Fig. 6). In our opinion, nanoparticle transcytotic access in dystrophic muscles results from the combined effects of NP-induced stimulation (NP effect) and the endothelial sensing machinery (EC effect). While the loss of endothelial dystrophin might contribute, we tend to believe that the "NP effect" is likely the dominant driver, as the observed "fold increase" became particularly dramatic for key transcytosis markers such as Rragd, Cadm4, and Depdc1a (Fig. 3D3).

Additionally, we explored the potential involvement of macrophages, a cell type specialized in particulate clearance. To investigate this, we performed a mechanistic experiment in mice, pre-

https://doi.org/10.1038/s41467-025-66061-8

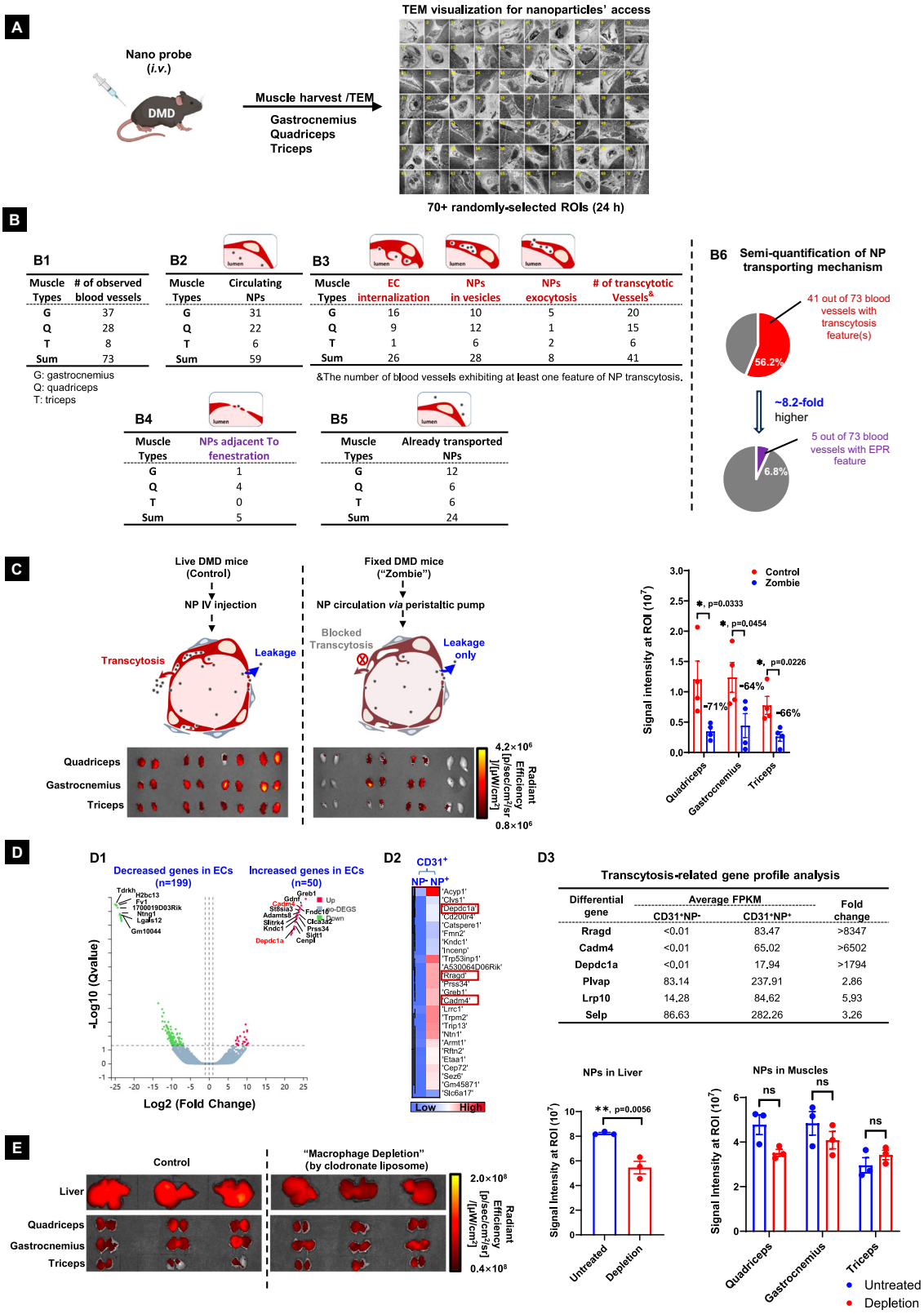

administering clodronate liposomes, which effectively deplete macrophages[50,51], prior to injecting NIR-labeled NPs. Our results suggest that macrophage depletion had a low to modest impact on NP accumulation in dystrophic muscles, such as the gastrocnemius and triceps (Fig. 3E). We observed a trend toward reduced particle biodistribution in the quadriceps (~20% reduction) following macrophage depletion, although this difference did not reach statistical significance. In contrast, depletion of liver-resident macrophages (Kupffer cells) led to a marked reduction in liver, underscoring the role of macrophage-mediated nanoparticle uptake in liver. This agreed with the extensive TEM analysis (Fig. 2D, E, Supplementary Data 1) and immunofluorescence staining (Supplementary Fig. 7), which revealed that a significant number of nanoparticles were not sequestered by macrophages inside muscles at 24 h post IV injection.

Fig. 3 | IV-injected NPs find their access to dystrophic muscle via a transcytosis-dominant mechanism. A Strategy of using gold-labeled lipid-coated NPs for identifying transcytosis in mdx mice based on more than 70 randomly selected ultrastructural tissue TEM regions-of-interest (ROIs) containing blood vessels. Created in BioRender. Meng, H. (2025) https://BioRender.com/vxg0ohj. **B** Within the aforementioned ROIs, a total of 37 gastrocnemius (G), 28 quadriceps (Q), and 8 triceps (T) vessels were analyzed (B1). Panel (B2) illustrates the quantification of circulating NPs within the blood vessels. Panel (B3) analyzed morphological aspects related to transcytosis, including internalization into ECs (2nd column), presence of NPs within intracellular vesicles of ECs (3rd column), and exocytosis from ECs (4th column). Panel (B4) computed the abundance of extravasated NPs in proximity to larger fenestrations. Additionally, Panel (B5) showed NPs that had already undergone transportation outside blood vessels. Panel (B6) depicts the relative frequency (%) of occurrences of transcytosis in contrast to the EPR effect across the entire ROIs. **C** Ex vivo imaging of muscles was conducted in live or fixed "Zombie" mice (B10-Dmd-KO) at 2 h after receiving IV injection or pump-circulation of NIR-labeled lipid-coated 70 nm MSNPs. The presented data represent mean ± SEM ($n = 4$ mice). **D** Gene expression of $CD31^+NP^+$ ECs (transcytosing ECs) compared to $CD31^+NP^-$ ECs ("quiescent" ECs) in gastrocnemius based on the RNA sequencing results from pooled 3 mice (B10-Dmd-KO). D1, Volcano plot showing the differentially expressed genes (DEGs) between the $CD31^+NP^+$ ECs versus $CD31^+NP^-$ ECs populations. D2, Heatmap of the relative gene expression of the 25 most over-expressed genes in transcytosing ECs compared to "quiescent" ECs with a Q value < 0.05. D3, Comparison of the expression levels (average FPKM) of genes related to the activation of transcytosis. **E** B10-Dmd-KO mice were pretreated with clodronate liposomes to deplete macrophages, followed by IV injection of NIR-labeled 70 nm NPs and sacrificed for ex vivo IVIS imaging at 24 h. Data are presented as mean ± SEM ($n = 3$ mice). Statistical analysis was performed using a two-tailed Student's t-test; $^*p < 0.05$, $^{**}p < 0.01$, ns not significant. Source data are provided as a Source data file.

This information collectively supported the discovery that transcytosis plays an important role in dystrophic muscles and prompted us to investigate the potential application of transcytotic-based drug delivery for DMD treatment.

Systemic delivery of tamoxifen using the transcytotic nanocarrier led to potent efficacy in dystrophic mice

To demonstrate the potential of transcytotic drug delivery in DMD, we encapsulated tamoxifen (TMX), a cancer drug, within our nanocarrier (Fig. 4A). TMX has shown promise in promoting endocrine crosstalk between the ER and ErbB1/ErbB2 signaling pathway, leading to ER phosphorylation and transcription of utrophin (Supplementary Fig. 8)[27]. Additionally, TMX reduces fibrosis through the TGF-β pathway[27,52]. From the chemical structure aspect, TMX is poorly soluble in water, and as a result, the commercial TMX is only available in an oral form[53]. Daily oral treatment for 15 months was required to achieve therapeutic outcomes[27].

We explored whether using our nanocarrier could overcome TMX's water solubility issue and achieve in vivo efficacy. We achieved this by soaking empty MSNP particles into the TMX ethanol solution. The hydrophobic nature of TMX, containing a tertiary amine, facilitated efficient drug attachment onto the silica surface, which contains silanol and carries a negative charge. This attachment occurred via combined hydrophobic and electrostatic interactions (Fig. 4B). To stabilize the drug-soaked MSNPs, we employed a lipid coating procedure that effectively sealed the silica pores, similar to Fig. 2A. The resulting formulation, termed "TMX NP," exhibited a drug loading capacity of 17.5% (w/w, drug/MSNP). The TMX NP's hydrodynamic size was 114.2 nm, and it carried a zeta potential of −8.83 mV (Fig. 4C). Then, dystrophic mice received IV TMX NP injection, followed by blood collection at different time points and LC-MS analysis of drug concentration in the plasma. This allowed us to determine the circulatory half-life, which was ~6.9 h post IV injection (Fig. 4D).

An efficacy study was performed using a total of 11 IV injections of TMX NP in male mice at drug dose of 10 mg/kg (particle dose: ~57 mg/kg; $n = 7$) (Fig. 4E). While the ideal comparison would have been the IV injection of free tamoxifen at an identical dose and frequency, it was technically infeasible due to the high amount of DMSO required for solubilizing the free drug. A reasonable compromise was made by including the daily oral administration of free TMX as a control by embedding TMX in the rodent diet, which was previously published to yield preclinical success in vivo[27].

Since the upregulation of utrophin expression, in this case through the use of free drug or TMX NP, is considered a potential therapeutic strategy to counteract the loss of dystrophin and improve muscle function in DMD[27,54], we measured utrophin expression using both immunoblotting and IF staining (Fig. 4F and Supplementary Figs. 9 and 10). We also quantified the results based on immunoblotting results ($n = 7$ per group). Our results demonstrated that treatment with TMX NPs led to increased utrophin expression in the gastrocnemius ($p = 0.0409$, Fig. 4F) and triceps ($p = 0.0082$, Supplementary Fig. 9A) muscles, compared to the free drug. A similar trend was observed in the quadriceps, where both free and TMX NPs outperformed saline, although the p-value did not reach statistical significance between the free drug and TMX NP groups (Supplementary Fig. 9B). To evaluate the anti-fibrotic effects of the indicated therapy, we performed Masson's trichrome (MT) staining and hydroxyproline (HYP) assay on various muscle samples. The results demonstrated better outcome of collagen reduction with TMX NPs treatment over the free drug, resulting in statistical significance (i.e., $p = 0.0254$ in gastrocnemius in Fig. 4G, $p = 0.0090$ in triceps, and $p = 0.0095$ in quadriceps in Supplementary Fig. 11).

Given the widespread use of hematoxylin-eosin (H&E) staining in clinical assessments, we employed H&E staining to quantitatively evaluate necrotic tissue areas, according to a published TREAT-NMD Network SOP[27,55]. This method allows for the differentiation between Type 1 damage (necrosis with an inflammatory component) and Type 2 damage (characterized by hypercontracted myofibers and degenerating myofibers). To minimize potential observer-induced bias, our standard procedure includes H&E staining, a full tissue scan (~5 × 5 mm in size), and ROI identification by the same trained pathologist across the entire tissue cross-section (Fig. 4H and Supplementary Figs. 12 and 13). We demonstrated that TMX NP exerted the most pronounced effect in terms of reducing the total necrotic area specifically in the gastrocnemius and quadriceps muscles (Fig. 4H and Supplementary Fig. 13A). In triceps, TMX NPs significantly reduced necrosis compared to saline control. While TMX NPs showed a trend of improvement over the free drug (Supplementary Fig. 13B), the p-value did not reach statistical significance. Moreover, muscle strength improvement was evaluated using the grip power test, following a published SOP for DMD preclinical studies[27,55]. Both free TMX and TMX NPs improved grip strength compared to saline. Notably, TMX NPs treatment resulted in further improvement compared to the free drug ($^{***}p = 0.0002$, Fig. 4I).

The safety of MSNP drug delivery is of key importance for DMD treatment. This includes the inherent biocompatibility of the carrier as well as any potential benefits that may accrue from the API. No major toxicity was discovered, evidenced by the overall animal health monitor including body weight change (Supplementary Fig. 14A), blood chemistry (Supplementary Fig. 14B), and the H&E histology evaluation on main organs such as heart, liver, spleen, lung, and kidneys (Supplementary Fig. 14C).

Discussions

In this communication, we discovered a transcytotic transport mechanism used by NPs to enter dystrophic muscle tissues after systemic delivery. The biodistribution of the nanocarrier can be markedly improved by size and surface design to ensure the colloidal stability

https://doi.org/10.1038/s41467-025-66061-8

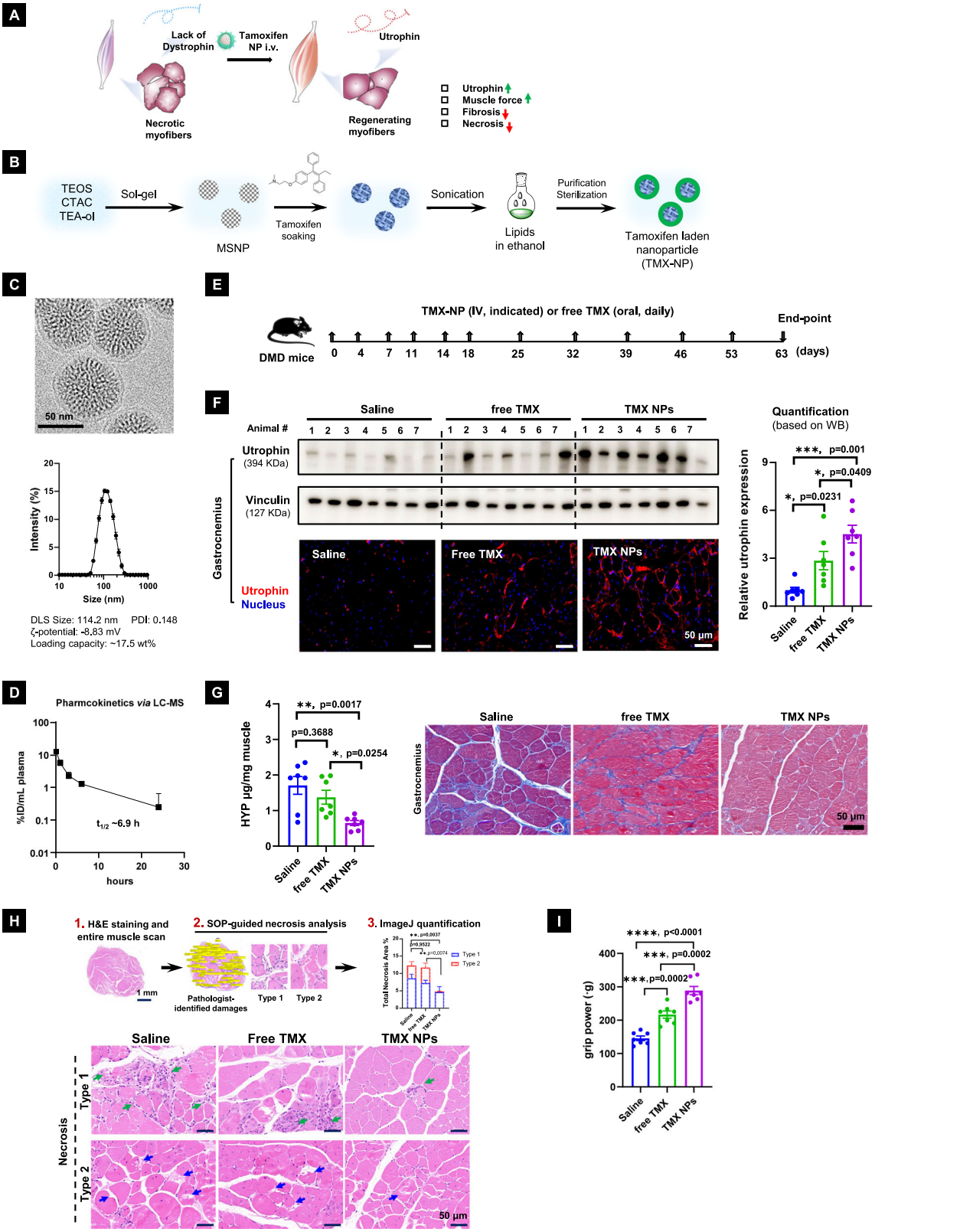

and homing efficiency to dystrophic skeletal muscles. An exciting discovery was the contrast in NP retention in dystrophic versus healthy muscle, accompanied by reduced NP content in liver and spleen. Instead of only observing NP extravasation through leaky vasculature, we also obtained ultrastructural, biochemical, and molecular evidence that the size-controlled nanocarrier finds its access to dystrophic muscle primarily through a transcytotic process. For proof-of-concept purposes only, IV administration of TMX NPs led to in vivo efficacy in dystrophic muscles.

Previous technologies using nanocarriers (such as liposomal, polymeric, and inorganic formulations) to deliver various payloads have not yet been approved for use in DMD patients[3,9,46,47]. These efforts usually remain at a preclinical stage, and there is very limited success with systemic delivery. A fundamental question at the nano/

Fig. 4 | Systemic administration of TMX NPs led to potent efficacy in a DMD mouse model. A Schematic to show systemic delivery of TMX NPs may lead to muscle function improvement by upregulating utrophin expression, accompanied by fibrosis and necrosis reduction. **B** Schematic to show the loading process of tamoxifen in lipids-coated MSNPs. **C** Characterization of TMX NPs for morphology, size, zeta potential, and loading capacity. **D** Pharmacokinetic (PK) profile of TMX NPs after IV injection ($n = 3$ mice). For (**C**, **D**), data are presented as mean ± SD ($n = 3$). **E** B10-Dmd-KO mice ($n = 7$ mice per group) received IV injections of TMX NPs at a drug dose of 10 mg/kg. The treatment schedule is outlined. Saline and daily oral administration of free TMX were used as controls. **F** Immunoblotting was performed to assess utrophin expression ($n = 7$ mice), along with representative immunofluorescence images (blue: nuclei; red: utrophin) in gastrocnemius muscles. Scale bar = 50 μm. Similar analyses were conducted for the quadriceps and triceps, as shown in Supplementary Fig. 9. **G** Fibrosis was evaluated using hydroxyproline (HYP) assays and Masson's trichrome collagen staining (blue: collagen) of gastrocnemius muscles. Scale bar = 50 μm. Data for the quadriceps and triceps are provided in Supplementary Fig. 11. **H** Necrosis in the gastrocnemius was evaluated through H&E staining for mice treated with free drug or TMX NPs. Representative images and semi-quantitative results are shown. Scale bar = 50 μm. H&E staining for the quadriceps and triceps is provided in Supplementary Fig. 13. **I** Muscle strength was assessed using a grip power test ($n = 7$ mice). For (**F**–**I**), data are presented as mean ± SEM ($n = 7$ mice). Statistical analysis was performed using one-way ANOVA followed by Dunnett's test; $^{*}p < 0.05$, $^{***}p < 0.001$, $^{****}p < 0.0001$. Source data are provided as a Source data file.

bio interface, therefore, becomes understanding the biochemical basis for how nanocarriers access the dystrophic microenvironment. Is the putatively enlarged fenestration in the inflamed tissue the only mechanism to interpret nanocarrier access in DMD? Noteworthy, while the size range of 50–100 nm could fit into the abnormal EC gaps, it is also in the same ballpark of various endocytic cellular compartments, such as VVO and macropinocytotic vesicles, which might play a role during the nutrition supply and vascular transcytosis[48,56–58]. For cancers, Sindhwani et al. demonstrated that up to 97% of gold-based nanoparticles enter solid tumors through transcytosis[18,19]. These recent discoveries were regarded as a "wake-up call" to rethink nanocarrier design in solid tumors[21]. In rare diseases like DMD, we have now reported the important role of transcytosis-mediated muscle access (Fig. 3B, C). In addition to the lipid-coated MSNP nanocarriers, we also extended our research to explore the transport of PEGylated gold nanoparticles, followed by TEM ultrastructural analysis. This investigation also revealed evidence of transcytotic vascular transport (Supplementary Fig. 15). Together, these data provide another demonstration of the enhanced transcytosis and retention (ETR) effect in a non-cancer setting, and our findings suggest a new path to design targeted nanomachines for muscle delivery[59,60].

Identifying the nanoparticle transportation mechanism within a heterogeneous and highly fibrotic biological environment is a technically challenging task. From a methodological standpoint, we recommend employing complementary approaches, including the zombie experiment, flow cytometry, EC cell sorting, and TEM analysis, to investigate NP transcytosis in dystrophic muscles and other organs where transcytosis may occur. The "pros" and "cons" of different approaches for studying NP transcytosis were summarized in Supplementary Table 1.

We also want to briefly comment on the limitations of the current work. Although we have highlighted the pivotal role of transcytosis in DMD drug delivery, our study did not investigate the formation of a biological "corona" on the nanocarrier surface[61]. We surmise that these corona molecules could form a "sandwich" structure, potentially activating downstream events. We would like to comment on the intramuscle nanoparticle distribution and in vivo drug release in the dystrophic muscles. It is possible that the effectiveness of TMX NPs does not necessarily depend on intracellular nanoparticle uptake. While our current research offers proof-of-concept data demonstrating the ability of small molecule delivery to dystrophic skeletal muscle, addressing additional biological barriers, such as the sarcolemma, will be crucial for nucleic acid delivery in this genetic disease. Another limitation of our study is the limited capacity to address cardiomyopathy and diaphragmatic myopathy in DMD, which could be a key focus for future iterations of this direction. In our study, we observed low nanoparticle uptake in the diaphragm, with particularly minimal accumulation in the heart. This phenomenon is likely driven by multiple factors, and we suspect that it is not exclusive to silica-based nanocarriers. For the diaphragm, its unique physiology with high collagen density, distinct vascular architecture, and continuous mechanical stress may limit the nanoparticles accumulation[62,63]. For the heart, one contributing factor could be the rapid cardiac blood flow, which limits the residence time of nanoparticles and reduces their opportunity to interact with the vascular endothelium[64,65]. Additionally, cardiomyocytes are terminally differentiated with minimal endocytic/vesicular activity[66,67] and are not inherently phagocytic, further restricting nanoparticle internalization. Their dense contractile machinery and mitochondrial/myofibrils volume further limit nanoparticle internalization[68]. One possible design was to incorporate targeting moieties like cardiomyocyte-targeting T9 peptide[69] or cell-penetrating peptides (Pip6)[70] to enhance biodistribution specifically to the heart. It is also possible to use phage display technology to identify diaphragm-targeting peptides, which could be employed to further functionalize nanocarriers for improved delivery. At the same time, it is necessary to balance design complexity with target efficiency, as excessive manufacturing complexity may raise difficulties in translation[71].

Methods

Materials

Tetraethylorthosilicate (TEOS, Cat# 86578), triethanolamine (TEA-ol, Cat# 90279), cetyltrimethylammonium chloride solution (CTAC, Cat# 292737), (3-aminopropyl)triethoxysilane (APTES, Cat# 440140), gold(III) chloride hydrate ($HAuCl_4 \cdot 3H_2O$, Cat# 520918), trisodium citrate dihydrate (Cat# S4641), and were purchased from Sigma-Aldrich. Lipids, including 1,2-distearoyl-sn-glycero-3-phosphocholine (DSPC, Cat# 850365), 1,2-distearoyl-sn-glycero-3-phosphoethanolamine-N-[methoxy (polyethylene glycol)-2000] (ammonium salt) (DSPE-PEG_{2000}, Cat# 880120), and cholesterol (Chol, Cat# 700000) were obtained from Avanti Polar Lipids. Tamoxifen citrate (Cat# T101373) was purchased from Aladdin. The following antibodies were used: anti-laminin polyclonal antibody (Sigma-Aldrich, Cat# L9393), anti-CD31 monoclonal antibody (clone 390, BD Pharmingen, Cat# 553708), anti-collagen IV polyclonal antibody (Abcam, Cat# ab19808), anti-alpha smooth muscle actin (α-SMA) monoclonal antibody (clone 1A4, Sigma-Aldrich, Cat# A5228), anti-utrophin monoclonal antibody (Santa Cruz Biotechnology, Cat# sc-33700), and anti-F4/80 monoclonal antibody (BioLegend, Cat# 122601). Secondary antibodies were purchased from Thermo Fisher Scientific, including Alexa Fluor® 488-conjugated goat anti-rat IgG (H+L) (Cat# A11006), Alexa Fluor® 594-conjugated goat anti-rat IgG (H+L) (Cat# A11007), Alexa Fluor® 488-conjugated goat anti-rabbit IgG (H+L) (Cat# A11008), and Alexa Fluor® 594-conjugated goat anti-rabbit IgG (H+L) (Cat# A11012). HRP-linked secondary antibodies, including anti-rabbit IgG (Cat# 7074) and anti-mouse IgG (Cat# 7076), were obtained from Cell Signaling Technology. DyLight 680 NHS ester (Cat# 46418) was acquired from Thermo Fisher Scientific. All chemicals were used as received without further purification.

Nanoparticle synthesis

To investigate the size effect of nanocarriers on biodistribution in the DMD mouse model, monodisperse spherical MSNPs with different primary size range from ~50 to ~300 nm were prepared. For systemic

administration, we also introduced the same lipid coating on the silica surface to maintain the colloidal stability in the biological environment. To monitor the particles via IVIS imaging or fluorescence microscopy, the MSNP core was labeled with an NIR dye. Briefly, the differently sized MSNPs were synthesized by a sol-gel chemistry using a seed-growth procedure[21,22]. Fifty nanometers of MSNP with a pore size of ~3 nm were synthesized with minor modifications as described in our previous reports[31]. Five milliliters of cetyltrimethylammonium chloride (CTAC, 25 wt% in water) solution was added to 15 mL of DI H_2O, followed by stirring at 500 rpm for 10 min at 85 °C. This was followed by the addition of 0.8 mL of 10% (w/v) triethanolamine (TEA-ol) for 10 min at the same temperature. Then, 1 mL of the silica precursor, tetraethylorthosilicate (TEOS), was added. The solution was stirred at 500 rpm at 85 °C for 1 h, leading to the formation of particles with a primary size of ~50 nm. Synthesis of larger MSNPs was performed in the same manner as making the 50 nm particles (serving as "seed"), but adding 1 mL of the above 50 nm seed particles to the mixture of CTAC and TEA-ol solution before adding the TEOS. The final particle size was controlled by adjusting the amount of TEOS in the growth step, which led to ~100, 200, and 300 nm MSNPs. The particles were extensively washed to remove the surfactant CTAC[31]. The purified MSNPs were modified with amino groups and further labeled by the NIR dye (DyLight 680 NHS ester, the dye: MSNP ratio is 0.1 wt.%)[15,31]. For lipid coating, the MSNPs were coated with a lipid bilayer (LB)[31,32]. A mixture of lipids (32 mg DSPC, 10.8 mg Chol, and 5.4 mg DSPE-PEG_{2000}, yielding a molar ratio of 3:2:0.15) was dissolved in 100 μL pure ethanol at ~65 °C. One mL of a preheated (~65 °C) solution, containing a 20 mg/mL NIR dye-labeled MSNP suspension, was added to the lipid solution and mixed by pipetting. The mixture was probe sonicated using a 10 s/5 s on/off cycle for 10 min. The particle suspension was purified by centrifugation and washing with PBS three times, which was further filtered through a 0.22 μm filter for sterilization. For detecting particles in tissue with TEM analysis, we also prepared MSNP with a gold core with high TEM contrast. In this case, the lipid-coated MSNPs with an ~10 nm gold core was synthesized by a three-step procedure as shown in our previous report[15], i.e., first make gold nanoparticles, then grow the mesoporous silica shell on the gold core to achieve the final size ~70 nm, and finally coat the MSNPs with lipid coating.

Nanoparticle characterization

The particle morphology is characterized using a transmission electron microscope (JEOL 1200-EX), and the coated LB on MSNPs was visualized by cryo-EM (TF20 FEI Tecnai-G2). The fluorescence spectra of labeled particles were measured by a Microplate Reader (M5e, Molecular Device, USA). Particle hydrodynamic size and zeta potential were measured by a ZETAPALS instrument (Brookhaven Instruments Corporation) or Zetasizer instrument (Dynamic Light Scattering, Malvern).

Animal study

All animal work was conducted under protocols approved by the institutional Animal Research Committees at the Chinese Academy of Sciences and UCLA. The mice were maintained under a 12-h dark/light cycle, with an ambient temperature of 20–26 °C and air humidity of 30–70%. The basic feed was purchased from SiPeiFu Biotechnology Co., Ltd. The main components include corn, soybean meal, fish meal, vitamins, trace elements, and amino acids, and then sterilized using 60Co irradiation. Tamoxifen-enriched feed is prepared by adding 100 mg/kg of tamoxifen (PSAITONG, cat: T80001) to the above-mentioned basic feed, which was customized and provided by Guangzhou Samo Bio-Tech Co., Ltd. Two DMD mouse models were used in this study: the classic mdx strain (C57BL/10ScSn-Dmd^{mdx}/J, Jackson Laboratory #001801)[72–74] and a dystrophin-deficient strain B10-Dmd-KO (C57BL/10ScSnJGpt-Dmd^{em3Cd4}/Gpt, GemPharmatech #T003035). The latter is a functionally comparable MDX model commonly used in DMD research[75,76]. It was generated via a frameshift mutation that results in loss of dystrophin function. The specific animal strain is indicated in the figure legend. Most DMD studies use male mice because DMD is an X-linked disorder that primarily affects males. Although DMD can occur in females, it is much rarer. Approximately 2.5–7.8% of female carriers exhibit muscle weakness, and symptoms are generally milder compared to those in affected males[77]. Therefore, this study utilized only male animals.

Biodistribution study

Two sets of experiments were performed to compare (1) the distribution of MSNPs with various sizes and (2) the muscle distribution between dystrophic vs wild-type mice. To demonstrate the biodistribution of various MSNPs, dystrophic or WT mice received IV injection of NPs at 50 mg/kg ($n = 3$–4 mice). At the indicated time points (1, 4, and 24 h) postinjection, animals were sacrificed and followed by ex vivo imaging of the excised different muscles and major organs. Immediately following IVIS imaging, gastrocnemius, quadriceps, triceps, and tibialis anterior muscles were embedded in OCT compound. Immunofluorescent staining included TrueBlack® Lipofuscin Autofluorescence Quencher (Biotium) and blocking buffer (0.2% gelatin, 3% BSA, 10% goat serum, 0.1% tween-20 in PBS) to improve signal-to-noise ratio in identifying MSNPs by epi-fluorescent (Zeiss Observer-1) and confocal (Zeiss LSM-780 and Leica SP8) microscopy. When necessary, we also stained blood vessel markers (CD31 and α-SMA), macrophage marker (F4/80), or myofiber structure marker (collagen IV and Laminin) to assist the analysis of the intramuscular distribution of our NPs.

Similar to the aforementioned experiment, we also aimed to investigate whether age influences the entry of NPs into muscles. In this case, WT mice and dystrophic mice, aged 8 weeks or 30 weeks, respectively, received IV injections of NIR dye-labeled nanoparticles at the same particle dose (50 mg/kg). After 24 h, mice were euthanized, and quadriceps, gastrocnemius, and triceps were resected for IVIS imaging.

To examine the potential impact of macrophages on NP accumulation in dystrophic muscles, a biodistribution study was performed with or without macrophage depletion. Specifically, DMD mice were intravenously injected with 200 μL of clodronate liposomes (4 mg/mL; SN-ML-E005, SunLipo NanoTech) 24 h prior to receiving NIR dye-labeled nanoparticles, followed by animal sacrifice for ex vivo IVIS imaging.

Ultrastructural analysis of the intramuscular delivery of nanoparticles through TEM viewing

In order to reveal NP's transportation mechanism in the dystrophic muscle, we repeated the biodistribution study using a gold-core labeled nanocarrier. Dystrophic mice (~3 months, $n = 3$) received an IV injection of 50 mg/kg of the Au-core marked NPs. At the indicated time points (1, 4, and 24 h) postinjection, animals were sacrificed, and gastrocnemius, quadriceps, and triceps muscle biopsies were collected, washed in PBS, and immediately fixed with 2.5% glutaraldehyde. Further sample preparation and sectioning were performed. After fixation in 1% OsO_4, the samples were dehydrated in propylene oxide and embedded in resin. Tissue slices of 60–80 nm thick were placed on copper grids and viewed under an electron microscope (JEM-2100plus).

"Zombie" model

To reveal the contribution of transcytosis, a "Zombie" model was established in dystrophic mice, according to a published protocol that was originally designed for cancer drug delivery[18]. For the Zombie group, mice underwent cardiac perfusion with a washing solution (1000 U/mL heparin sodium in PBS) for 20 min using a peristaltic pump (L100-1S-1, LongerPump, China). The perfusion effluent was

preserved at 4 °C. Subsequently, the mice were carefully positioned to allow the flow back of the fixation solution (4% formaldehyde and 0.5% glutaraldehyde in PBS). After 1 h, the solution was replaced with a washing solution for an additional 20 min to remove any remaining fixation solution. The collecting tubes were then washed, and a nanoparticle solution (5x volume of NPs in perfusion effluent, i.e., 750 µL) was circulated for 2 h at a physiologically relevant flow rate (5–7 mL/min). For the control group, dystrophic mice received an IV injection of NPs. After 2 h, they underwent cardiac perfusion with a washing solution for 20 min, followed by the fixation solution for 1 h. Quadriceps, gastrocnemius, and triceps were then resected from these mice for IVIS imaging.

Flow cytometry analysis

The gastrocnemius muscle was dissected and processed into a single-cell solution using the Mouse Muscle Tissue Mild Enzymatic Hydrolysis Kit (RWD, DHME-10) following the manufacturer's instructions. Subsequently, the cell suspension was filtered through a 70 µm cell filter, and any remaining RBCs were removed using RBC Lysis Buffer (Biolegend, 420301). The suspension was then labeled with 5 µL of FITC anti-CD31 Rat Monoclonal Antibody per sample (Biolegend, clone: MEC13.3, 102506) for 30 min. Before performing the flow cytometry analysis, the samples were stained with 7-AAD Viability Staining Solution (Biolegend, 420403).

Cell sorting

To isolate the NP positive (NP^+) and negative (NP^-) cells, we extracted the cells as mentioned above. Cell sorting was achieved via a Fluorescence Flow Cytometry Sorting System (MoFlo XDP, Beckman Coulter). The muscle ECs were sorted into two populations: $CD31^+NP^+$ (Dy680+, APC channel) and $CD31^+NP^-$ in PBS before immediate transfer into TRIzol and delivered to a core facility (Beijing Genomics Institution, BGI Genomics) for RNA sequencing.

RNA sequencing and analysis

The RNA extraction, RNA library preparation, sequencing, and initial data analysis were done by BGI. $CD31^+$ NP^+ and $CD31^+$ NP^- muscle ECs of gastrocnemius from three different mdx mice were used and pooled together, respectively, for the sequencing. RNA extraction was done according to the standard procedure. The gene hit counts were used for differential expression analysis using DESeq2. The test was used to generate log2-fold change and Q-values. Genes that had a log2-fold change >1 and an adjusted Q value ≤ 0.05 were named as differentially expressed genes. The list of up-regulated genes in NP^+ muscle ECs was analyzed for gene ontology enrichment.

Demonstration of the efficacy of transcytotic tamoxifen delivery in vivo

In order to demonstrate the impact of drug delivery through a transcytotic nanocarrier mechanism, we used lipid-coated MSNP for systemic delivery of a highly insoluble drug, TMX, which was recently repurposed for DMD management. Briefly, TMX was soaked into MSNP, followed by lipid coating, purification, and characterization before IV injection.

To prepare tamoxifen-laden nanoparticles (TMX NPs), tamoxifen was first loaded in MSNPs (~70 nm) and then coated with the LB as described above. Briefly, tamoxifen (20 mg, 10 mg/mL dissolved in ethanol) was added to MSNP (40 mg, 63 mg/mL in ethanol), mixed and stirred overnight at room temperature. To remove the free tamoxifen, the mixture was centrifuged at 21,000 × g for 15 min, then the tamoxifen-MSNP pellet was resuspended in PBS by bath sonication. The tamoxifen-MSNP suspension was then transferred to a lipid ethanol solution, followed by probe sonication for further lipid coating. The final TMX NPs were purified by washing and centrifugation in PBS and filtered with a 0.22 µm sterile membrane. To determine the tamoxifen concentration in the TMX NPs, the particle solution was diluted 1/100 in pure ethanol before the absorbance was measured at 285 nm for tamoxifen (Spark, TECAN). The lipid coating, hydrodynamic diameter, and zeta potential of TMX NPs were characterized by cryo-EM and dynamic light scattering, respectively.

To characterize the pharmacokinetics of TMX NPs, male dystrophic mice (n = 3) received a single IV injection of TMX NPs at a TMX dose of 10 mg/kg. The blood samples were collected at 5 min, 1, 3, 6, and 24 h. After separation of the plasma fraction, drugs were extracted with acetonitrile (plasma: acetonitrile 1:4 v/v) followed by vigorous shaking in a tissue homogenizer (QIAGEN, TissueLyser II). The plasma suspensions were then centrifuged at 16000 × g at 4 °C for 10 min. The supernatant was filtered through a 0.22 µm sterile membrane before being loaded to Liquid Chromatography/Mass Spectrometry (LC/MS). The LC/MS (Agilent, 6495C) analysis condition: LC was performed using a Symmetry C18 column (Waters, WAT045905, 4.6 × 150 mm) at a flow rate of 1.0 mL/min, injection volume of 10 µL, 280 nm absorbance wavelength, and a temperature of 30 °C. The LC mobile phase was grade acetonitrile/H_2O (50:50 ratio, isocratic). Concentrations of TMX were calculated by determining the area under the curve, using a calibration curve that was established by known concentrations of the standard Tamoxifen compound. The following transitions were used for MRM acquisition: TMX m/z 372-72 (quantitation). The PK data were fitted in a one-compartment model, using PKSolver software[78].

For the efficacy study, male mice (~3 months) received a total of 11 IV injections (n = 7 mice) as we outlined in Fig. 4E. The TMX and MSNP doses were 10 mg/kg and 57 mg/kg, respectively. The controls include saline (n = 7 mice) or free drug (n = 7 mice). The poor TMX water solubility prevents us from including free drug control (IV), as we clarified in the manuscript. Instead, a TMX-containing rodent diet (100 mg drug/kg food) was used for daily oral administration of free tamoxifen (~10 mg/kg), using a published protocol in the literature[27]. During the treatment, animal health conditions were monitored. At the conclusion stage of the experiment, the muscle strength improvement was evaluated by the grip power test[27]. Muscle strength was measured by the grip power test using a Mouse Grip Tester (Model YLS-13A, Jinan Yiyan Tech Co., LTD). Briefly, each mouse was gently placed on the instrument, and its tail was pulled at a constant speed in a horizontal direction. The instrument recorded the maximum pull force. This procedure was repeated four times per mouse, and the average value was calculated. Then, the animals were sacrificed, the gastrocnemius, quadriceps, and triceps muscles, and other main organs were collected and fixed in 10% formalin for 48 h before being paraffin-embedded. The 6 µm-thick transverse sections were performed with MT staining or H&E staining dye according to standard procedures via an automatic dying machine (DRS-Prisma-P-JCS&Film-JC2, SAKURA, Japan). To quantify the histopathology in the above-mentioned stained muscle sections, the entire cross-sectional areas of muscles were scanned and analyzed. Histological features were identified manually by the researcher and quantified using image analysis software (SlideViewer, 3DHISTECH Ltd., v2.6.0). To quantitate the abundance of a specific histological feature (e.g., myofiber necrosis of Type 1 damage with an inflammatory component or Type 2 of hypercontracted myofibers and degenerating myofibers) per muscle cross-sectional area, the areas were drawn around to get an absolute value (µm2). The area% was calculated as abnormal area / whole area. Histological features were identified according to the TREAT-NMD protocol DMD_M.1.2.007 (Quantification of histopathology in H&E stained muscle sections)[27,55].

For utrophin immunoblotting, muscle tissues were homogenized in RIPA buffer containing protease inhibitors. Equal amounts of total protein (40 µg) from muscle extracts were loaded onto 6% Tris-Acetate gels and transferred to a 0.45 µm PVDF membrane over 6.5 h. Membranes were blocked with 5% milk in TBST for 1 h and incubated with primary antibodies against utrophin (1:300, sc-33700, Santa Cruz) or vinculin (1:100,000, A2752, Abclonal). Protein bands were visualized

using a chemiluminescence detection system (Amersham ImageQuant800, Cytiva) and quantified using ImageJ software. For immunofluorescence staining for utrophin, 6 μm-thick transverse paraffin sections were obtained as mentioned above. After dewaxing and rehydration, 3% H_2O_2 solution in methanol was used to block endogenous peroxidase activity at room temperature for 10 min. Next, antigen retrieval was performed using a citrate buffer (10 mM citrate buffer, pH = 6.0) at 95–100 °C for 10 min. The sections were then blocked in 5% BSA in PBS for 60 min at 37 °C, followed by incubation with primary antibody (monoclonal antibody, sc-33700, Santa Cruz) overnight and Alexa Fluor 488-conjugated secondary antibody for 60 min. Images were finally viewed and captured under a confocal microscope (A1 HD25, Nikon). Section images were scanned with a research slide scanner (SLIDEVIEW VS200, Olympus).

Muscle fibrosis, indicated by collagen content, was quantified using a hydroxyproline assay kit (A030-2-1, Nanjing Jiancheng Biotechnology Co., Ltd.). Moreover, to further assess the biosafety of TMX NP, the levels of alanine aminotransferase (ALT), aspartate aminotransferase (AST), blood urea nitrogen (BUN), and creatinine (CRE) were measured.

Statistical analysis

Comparative analysis of differences between groups was performed using the two-tailed Student's *t*-test (Excel software, Microsoft) for two-group comparison. A One-way ANOVA test was performed for multiple group comparisons on Prism 7 software (GraphPad). Data were expressed as mean ± SD or SEM, as stated in the figure legends. A statistically significant difference was considered at $p < 0.05$.

Ethics statement

All animal experiments were performed following the ARRIVE guidelines for the reporting of in vivo studies and conducted under protocols approved by the institutional Animal Research Committees at the Chinese Academy of Sciences (2022R0014 and AP2024-08-0097) and the University of California, Los Angeles (ARC 2006-119-31A). All the animal studies utilized only male animals, given the biological relevance to DMD, an X-linked disorder that predominantly affects males.

Reporting summary

Further information on research design is available in the Nature Portfolio Reporting Summary linked to this article.

Data availability

The data supporting the findings of the study are included in the main text and supplementary information files. The summary of all the original muscle TEM images has been provided as Supplementary Data 1 and 2. The RNA-seq data generated in this study have been deposited in the NCBI Sequence Read Archive (SRA) under accession code PRJNA1068853. Source data are available in a Source data file. Source data are provided with this paper.

References

1. Wang, J., Li, Y. & Nie, G. Multifunctional biomolecule nanostructures for cancer therapy. *Nat. Rev. Mater.* **6**, 766–783 (2021).
2. Zhang, C. et al. Progress, challenges, and future of nanomedicine. *Nano Today* **35**, 101008 (2020).
3. Nance, M. E., Hakim, C. H., Yang, N. N. & Duan, D. Nanotherapy for Duchenne muscular dystrophy. *Wiley Interdiscip. Rev. Nanomed. Nanobiotechnol.* **10**, e1472 (2018).
4. Xie, X. et al. Interleukin–10 plasmid delivery by polymeric nanocarrier shows efficient and safe tissue repair in acute muscle damage models in mice. *Nano Today* **46**, 101544 (2022).
5. Yang, P. et al. Nano-vectors for CRISPR/Cas9-mediated genome editing. *Nano Today* **44**, 101482 (2022).
6. Verhaart, I. E. & Aartsma-Rus, A. Therapeutic developments for Duchenne muscular dystrophy. *Nat. Rev. Neurol.* **15**, 373–386 (2019).
7. Hodgson, J. Drug pipeline 2Q23 - controversy and complexity. *Nat. Biotechnol.* **41**, 1041–1043 (2023).
8. Kishimoto, T. K. & Samulski, R. J. Addressing high dose AAV toxicity —'one and done' or 'slower and lower'? *Expert Opin. Biol. Ther.* **22**, 1067–1071 (2022).
9. Falzarano, M. S., Passarelli, C. & Ferlini, A. Nanoparticle delivery of antisense oligonucleotides and their application in the exon skipping strategy for Duchenne muscular dystrophy. *Nucleic Acid Ther.* **24**, 87–100 (2014).
10. Emami, M. R. et al. Polyrotaxane nanocarriers can deliver CRISPR/Cas9 plasmid to dystrophic muscle cells to successfully edit the DMD gene. *Adv. Ther.* **2**, 1900061 (2019).
11. Lee, K. et al. Nanoparticle delivery of Cas9 ribonucleoprotein and donor DNA in vivo induces homology-directed DNA repair. *Nat. Biomed. Eng.* **1**, 889–901 (2017).
12. Randolph, M. E. & Pavlath, G. K. A muscle stem cell for every muscle: variability of satellite cell biology among different muscle groups. *Front. Aging Neurosci.* **7**, 190 (2015).
13. Khlebtsov, N. & Dykman, L. Biodistribution and toxicity of engineered gold nanoparticles: a review of in vitro and in vivo studies. *Chem. Soc. Rev.* **40**, 1647–1671 (2011).
14. Bourquin, J. et al. Biodistribution, clearance, and long-term fate of clinically relevant nanomaterials. *Adv. Mater.* **30**, e1704307 (2018).
15. Liu, X. et al. Tumor-penetrating peptide enhances transcytosis of silicasome-based chemotherapy for pancreatic cancer. *J. Clin. Investig.* **127**, 2007–2018 (2017).
16. Liu, X., Jiang, J. & Meng, H. Transcytosis—an effective targeting strategy that is complementary to "EPR effect" for pancreatic cancer nano drug delivery. *Theranostics* **9**, 8018–8025 (2019).
17. Zhou, Q. et al. Enzyme-activatable polymer-drug conjugate augments tumour penetration and treatment efficacy. *Nat. Nanotechnol.* **14**, 799–809 (2019).
18. Sindhwani, S. et al. The entry of nanoparticles into solid tumours. *Nat. Mater.* **19**, 566–575 (2020).
19. Kingston, B. R. et al. Specific endothelial cells govern nanoparticle entry into solid tumors. *ACS Nano* **15**, 14080–14094 (2021).
20. Ruoslahti, E. Access granted: iRGD helps silicasome-encased drugs breach the tumor barrier. *J. Clin. Investig.* **127**, 1622–1624 (2017).
21. de Lazaro, I. & Mooney, D. J. A nanoparticle's pathway into tumours. *Nat. Mater.* **19**, 486–487 (2020).
22. Nguyen, L. N. et al. The mechanisms of nanoparticle delivery to solid tumours. *Nat. Rev. Bioeng.* **2**, 201–213 (2024).
23. Wu, J. L. et al. The pathways for nanoparticle transport across tumour endothelium. *Nat. Nanotechnol.* **20**, 672–682 (2025).
24. Zhou, L. & Lu, H. Targeting fibrosis in Duchenne muscular dystrophy. *J. Neuropathol. Exp. Neurol.* **69**, 771–776 (2010).
25. Briguet, A. et al. Histological parameters for the quantitative assessment of muscular dystrophy in the mdx-mouse. *Neuromuscul. Disord.* **14**, 675–682 (2004).
26. Feig, C. et al. The pancreas cancer microenvironment. *Clin. Cancer Res.* **18**, 4266–4276 (2012).
27. Dorchies, O. M. et al. The anticancer drug tamoxifen counteracts the pathology in a mouse model of Duchenne muscular dystrophy. *Am. J. Pathol.* **182**, 485–504 (2013).
28. Gayi, E. et al. Repurposing the selective oestrogen receptor modulator tamoxifen for the treatment of Duchenne muscular dystrophy. *Chimia* **72**, 238–240 (2018).
29. Markati, T. et al. Emerging therapies for Duchenne muscular dystrophy. *Lancet Neurol.* **21**, 814–829 (2022).
30. Meng, H. et al. Use of a Lipid-coated mesoporous silica nanoparticle platform for synergistic gemcitabine and paclitaxel delivery to human pancreatic cancer in mice. *ACS Nano* **9**, 3540–3557 (2015).

31. Liu, X. et al. Irinotecan delivery by lipid-coated mesoporous silica nanoparticles shows improved efficacy and safety over liposomes for pancreatic cancer. *ACS Nano* **10**, 2702–2715 (2016).
32. Liu, X. et al. Improved efficacy and reduced toxicity using a custom-designed irinotecan-delivering silicasome for orthotopic colon cancer. *ACS Nano* **13**, 38–53 (2019).
33. Ji, Y. et al. Use of ratiometrically designed nanocarrier targeting CDK4/6 and autophagy pathways for effective pancreatic cancer treatment. *Nat. Commun.* **11**, 4249 (2020).
34. Liu, X. et al. Combination chemo-immunotherapy for pancreatic cancer using the immunogenic effects of an irinotecan silicasome nanocarrier plus Anti-PD-1. *Adv. Sci.* **8**, 2002147 (2021).
35. Liu, X. et al. Development of facile and versatile platinum drug delivering silicasome nanocarriers for efficient pancreatic cancer chemo-immunotherapy. *Small* **17**, e2005993 (2021).
36. Ashley, C. E. et al. The targeted delivery of multicomponent cargos to cancer cells by nanoporous particle-supported lipid bilayers. *Nat. Mater.* **10**, 389–397 (2011).
37. Croissant, J. G. et al. Synthetic amorphous silica nanoparticles: toxicity, biomedical and environmental implications. *Nat. Rev. Mater.* **5**, 886–909 (2020).
38. Moeller, K., Kobler, J. & Bein, T. Colloidal suspensions of nanometer-sized mesoporous silica. *Adv. Funct. Mater.* **17**, 605–612 (2007).
39. Yamada, H. et al. Preparation of aqueous colloidal mesostructured and mesoporous silica nanoparticles with controlled particle size in a very wide range from 20 nm to 700 nm. *Nanoscale* **5**, 6145–6153 (2013).
40. Yamamoto, E. et al. Preparation of size-controlled monodisperse colloidal mesoporous silica nanoparticles and fabrication of colloidal crystals. *Chem. Mater.* **26**, 2927–2933 (2014).
41. Almeida, J. P., Chen, A. L., Foster, A. & Drezek, R. In vivo biodistribution of nanoparticles. *Nanomedicine* **6**, 815–835 (2011).
42. Yu, T., Hubbard, D., Ray, A. & Ghandehari, H. In vivo biodistribution and pharmacokinetics of silica nanoparticles as a function of geometry, porosity and surface characteristics. *J. Control. Release* **163**, 46–54 (2012).
43. Fu, C. et al. The absorption, distribution, excretion and toxicity of mesoporous silica nanoparticles in mice following different exposure routes. *Biomaterials* **34**, 2565–2575 (2013).
44. Kumar, M., Kulkarni, P., Liu, S., Chemuturi, N. & Shah, D. K. Nanoparticle biodistribution coefficients: a quantitative approach for understanding the tissue distribution of nanoparticles. *Adv. Drug Deliv. Rev.* **194**, 114708 (2023).
45. Hicks, M. R. et al. Nanoparticles systemically biodistribute to regenerating skeletal muscle in DMD. *J. Nanobiotechnol.* **21**, 303 (2023).
46. Bibee, K. P. et al. Rapamycin nanoparticles target defective autophagy in muscular dystrophy to enhance both strength and cardiac function. *FASEB J.* **28**, 2047–2061 (2014).
47. Wang, M. et al. Pluronic-PEI copolymers enhance exon-skipping of 2′-O-methyl phosphorothioate oligonucleotide in cell culture and dystrophic mdx mice. *Gene Ther.* **21**, 52–59 (2014).
48. Tuma, P. & Hubbard, A. L. Transcytosis: crossing cellular barriers. *Physiol. Rev.* **83**, 871–932 (2003).
49. Ramos, C. J. & Antonetti, D. A. The role of small GTPases and EPAC-Rap signaling in the regulation of the blood-brain and blood-retinal barriers. *Tissue Barriers* **5**, e1339768 (2017).
50. Tavares, A. J. et al. Effect of removing Kupffer cells on nanoparticle tumor delivery. *Proc. Natl. Acad. Sci. USA* **114**, E10871–E10880 (2017).
51. Lin, Z. P. et al. Macrophages actively transport nanoparticles in tumors after extravasation. *ACS Nano* **16**, 6080–6092 (2022).
52. Guiraud, S. & Davies, K. E. Pharmacological advances for treatment in Duchenne muscular dystrophy. *Curr. Opin. Pharmacol.* **34**, 36–48 (2017).
53. Buchanan, C. M. et al. Solubilization and dissolution of tamoxifen-hydroxybutenyl cyclodextrin complexes. *J. Pharm. Sci.* **95**, 2246–2255 (2006).
54. Miura, P. & Jasmin, B. J. Utrophin upregulation for treating Duchenne or Becker muscular dystrophy: How close are we? *Trends Mol. Med.* **12**, 122–129 (2006).
55. Nagaraju, K. & Willmann, R. Developing standard procedures for murine and canine efficacy studies of DMD therapeutics: report of two expert workshops on "Pre-clinical testing for Duchenne dystrophy": Washington DC, October 27th-28th 2007 and Zurich, June 30th-July 1st 2008. *Neuromuscul. Disord.* **19**, 502–506 (2009).
56. Baluk, P. et al. Endothelial gaps: time course of formation and closure in inflamed venules of rats. *Am. J. Physiol.* **272**, L155–L170 (1997).
57. Dvorak, H. F., Nagy, J. A., Feng, D., Brown, L. F. & Dvorak, A. M. Vascular permeability factor/vascular endothelial growth factor and the significance of microvascular hyperpermeability in angiogenesis. *Curr. Top. Microbiol. Immunol.* **237**, 97–132 (1999).
58. Nagy, J. A., Benjamin, L., Zeng, H., Dvorak, A. M. & Dvorak, H. F. Vascular permeability, vascular hyperpermeability and angiogenesis. *Angiogenesis* **11**, 109–119 (2008).
59. Qin, M., Feng, Z. & Meng, H. Enhanced transcytosis and retention (ETR) effect. *Sci. Bull.* **69**, 3640–3643 (2024).
60. Liu, Y. et al. Unlocking tumor barrier: annexin A2-mediated transcytosis boosts drug delivery in pancreatic and breast tumors. *Nat. Commun.* **16**, 6531 (2025).
61. Casals, E., Vitali, M. & Puntes, V. The nanoparticle-protein corona untold history (1907–2007). *Nano Today* **58**, 102435 (2024).
62. Stuelsatz, P., Keire, P., Almuly, R. & Yablonka-Reuveni, Z. A contemporary atlas of the mouse diaphragm: myogenicity, vascularity, and the Pax3 connection. *J. Histochem. Cytochem.* **60**, 638–657 (2012).
63. Wohlgemuth, R. P. et al. The extracellular matrix of dystrophic mouse diaphragm accounts for the majority of its passive stiffness and is resistant to collagenase digestion. *Matrix Biol. Plus* **18**, 100131 (2023).
64. Duncker, D. J. & Bache, R. J. Regulation of coronary blood flow during exercise. *Physiol. Rev.* **88**, 1009–1086 (2008).
65. Sahoo, S., Kariya, T. & Ishikawa, K. Targeted delivery of therapeutic agents to the heart. *Nat. Rev. Cardiol.* **18**, 389–399 (2021).
66. Ahuja, P., Sdek, P. & MacLellan, W. R. Cardiac myocyte cell cycle control in development, disease, and regeneration. *Physiol. Rev.* **87**, 521–544 (2007).
67. Essandoh, K., Teuber, J. P. & Brody, M. J. Regulation of cardiomyocyte intracellular trafficking and signal transduction by protein palmitoylation. *Biochem. Soc. Trans.* **52**, 41–53 (2024).
68. Barth, E., Stämmler, G., Speiser, B. & Schaper, J. Ultrastructural quantitation of mitochondria and myofilaments in cardiac muscle from 10 different animal species including man. *J. Mol. Cell. Cardiol.* **24**, 669–681 (1992).
69. Seow, Y., Yin, H. & Wood, M. J. Identification of a novel muscle targeting peptide in mdx mice. *Peptides* **31**, 1873–1877 (2010).
70. Betts, C. et al. Pip6-PMO, a new generation of peptide-oligonucleotide conjugates with improved cardiac exon skipping activity for DMD treatment. *Mol. Ther. Nucleic Acids* **1**, e38 (2012).
71. Mahmud, M. M., Pandey, N., Winkles, J. A., Woodworth, G. F. & Kim, A. J. Toward the scale-up production of polymeric nanotherapeutics for cancer clinical trials. *Nano Today* **56**, 102314 (2024).
72. Young, C. S. et al. A single CRISPR-Cas9 deletion strategy that targets the majority of DMD patients restores dystrophin function in hiPSC-derived muscle cells. *Cell Stem Cell* **18**, 533–540 (2016).
73. Hicks, M. R. et al. ERBB3 and NGFR mark a distinct skeletal muscle progenitor cell in human development and hPSCs. *Nat. Cell Biol.* **20**, 46–57 (2018).

74. Sicinski, P. et al. The molecular basis of muscular dystrophy in the mdx mouse: a point mutation. *Science* **244**, 1578–1580 (1989).
75. Zheng, J. et al. Satellite cell-specific deletion of Cipc alleviates myopathy in mdx mice. *Cell Rep.* **39**, 110939 (2022).
76. Zhang, R. X. et al. FNDC1 is a myokine that promotes myogenesis and muscle regeneration. *EMBO J.* **44**, 30–53 (2025).
77. Cho, Y. N. & Choi, Y. C. Female carriers of Duchenne muscular dystrophy. *J. Genet. Med.* **10**, 94–98 (2013).
78. Zhang, Y., Huo, M., Zhou, J. & Xie, S. PKSolver: an add-in program for pharmacokinetic and pharmacodynamic data analysis in Microsoft Excel. *Comput. Methods Programs Biomed.* **99**, 306–314 (2010).

Acknowledgements

This work was supported by the National Key Research and Development Program of China (2022YFA1207300 for H.M., 2021YFA1200902 for H.M.), the National Natural Science Foundation of China (32201143 for X.L., 32471438 for X.L., 32271452 for H.M., 82204300 for M.Q., 32571618 for M.Q.), and CAS Project for Young Scientists in Basic Research (YSBR-036 for H.M.). X.L. is thankful for the start-up funding support from Zhejiang Cancer Hospital, Hangzhou Institute of Medicine (HIM), Chinese Academy of Sciences (CAS). H.M. thanks the start-up packages of the National Center for Nanoscience and Technology, and the CAS Innovation team science award. The work was also partially supported by CIRM QUEST (#DISC2-08824 for A.D.P.). The authors would like to thank Jane Wen, Ekaterina Mokanova, Qikai Wang, and Yibo Li for technical assistance. The authors acknowledge the support from the Shared Instrumentation Core Facility, HIM, and CAS.

Author contributions

X.L., M.R.H., M.J.S., A.D.P., and H.M. conceived the research. X.L., M.R.H., Z.F., and J.J. designed and performed the experiments. C.S.Y., J.J., T.Z., K.S., M.R.E., M.Q., Y.L., J.L., Y.Z., H.Y., and Y.L. performed the experiments. X.L., M.R.H., Z.F., and J.J. analyzed the data. All the authors were involved in the data discussion. X.L., M.R.H., Z.F., J.J., M.J.S., A.D.P., and H.M. wrote the manuscript. The final manuscript was edited and approved by all authors.

Competing interests

The authors declare no competing interests.

Additional information

Supplementary information The online version contains supplementary material available at https://doi.org/10.1038/s41467-025-66061-8.

Correspondence and requests for materials should be addressed to Melissa J. Spencer, April D. Pyle or Huan Meng.

Peer review information *Nature Communications* thanks the anonymous reviewers for their contribution to the peer review of this work. A peer review file is available.